Geophysical Research Letters

Supporting Information for

Constraining the mechanisms of aeolian bedform formation on Mars through a global morphometric survey: Supporting information S1

David A. Vaz[1], Simone Silvestro[2,3], Matthew Chojnacki[4] and David C. A. Silva[1]

[1]Centre for Earth and Space Research of the University of Coimbra, Observatório Geofísico e Astronómico da Universidade de Coimbra, Coimbra, Portugal.

[2]INAF Osservatorio Astronomico di Capodimonte, Napoli, Italia.

[3]SETI Institute, Carl Sagan Center, Mountain View, CA, USA.

[4]Planetary Science Institute, Lakewood, CO, USA.

Contents of this file

Introduction

This file includes a detailed explanation of the applied methods, auxiliary data, supplementary figures and tables.

Text S1.

1. DATA AND GLOBAL BEFORM SURVEYS

To investigate the relation between atmospheric pressure (as function of elevation) and the wavelength of Martian large ripples we analyze a total of 75 HiRISE images (Table S1), some of which were previously surveyed by other authors. Namely, the first 11 areas

are the same reported by Lapotre et al. (2016), while the last 25 areas are the same analyzed by Lorenz et al. (2014) in the Tharsis region. We provide a complete mapping of the HiRISE images, extending the elevation coverage (Fig. S1b) and filling the gaps of previous works.

The new areas were selected based on the presence of dark-toned dunes or sand sheets which are covered by large ripples. Besides the Tharsis cluster that corresponds to the Lorenz et al. (2014) dataset, the selected areas are scattered across Mars surface (Fig. S1a). We primarily use full resolution HiRISE data (0.25 m/pix), although 0.5 m/pix images were used in five areas (this coarser spatial resolution is still enough to identify and map large ripples).

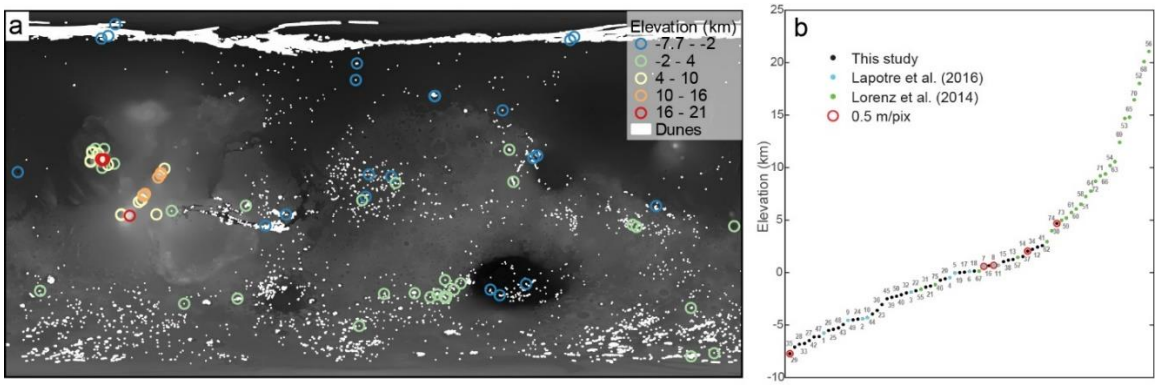

Fig. S1 – Global map and elevation distribution of the study areas. a) Location of the study areas, the global distribution of dune fields is shown in white (Fenton, 2020; Hayward et al., 2013). b) Elevations of the mapped areas, the different colors highlight the areas which were analyzed in previous studies (Lapotre et al., 2016; Lorenz et al., 2014); the numbers next to each dot correspond to the IDs in Table 1; areas where lower resolution 50 cm/pixel data were used are also noted. In this study we extend the sampled elevation range and provide more continuous coverage.

Table S1 – List of surveyed areas, including their location and spatial resolution. A full record of the information compiled in this study can be found at https://doi.org/10.6084/m9.figshare.21064657.

Area ID	Image	Spatial resolution (m/pix)	Location	Previous studies
1	ESP_027864_2295_RED	0.25	Acidalia Mensa	Lapotre et al. 2016
2	ESP_018854_1755_RED	0.25	Gale crater	Lapotre et al. 2016
3	ESP_034909_1755_RED	0.25	Juventae Chasma	Lapotre et al. 2016
4	ESP_025042_1375_RED	0.25	SE of Yaonis Regio	Lapotre et al. 2016
5	ESP_011421_1300_RED	0.25	Hellespontus	Lapotre et al. 2016
6	ESP_041987_1340_RED	0.25	Proctor crater	Lapotre et al. 2016
7	ESP_011909_1320_RED	0.50	SE of Proctor crater	Lapotre et al. 2016
8	ESP_024502_1305_RED	0.50	SW of Proctor crater	Lapotre et al. 2016
9	PSP_001970_1655_RED	0.25	Coprates Chasma	Lapotre et al. 2016
10	ESP_018011_2565_RED	0.25	North Polar erg	Lapotre et al. 2016
11	ESP_039955_1875_RED	0.25	S of Nili Patera	Lapotre et al. 2016
12	ESP_013790_1035_RED	0.25	Planum Australe	
13	ESP_049439_1165_RED	0.25	Sisyphi Planum	
14	ESP_023913_1275_RED	0.25	Thaumasia	
15	ESP_021509_1325_RED	0.25	Kaiser Crater	
16	ESP_048154_1255_RED	0.25	S Eridania	
17	ESP_022320_1335_RED	0.25	Terra Sirenum	
18	ESP_022422_1300_RED	0.25	Ogygis Undae	
19	ESP_032941_1310_RED	0.25	Noachis Terra	
20	ESP_019570_1390_RED	0.25	North of Rabe Crater	
21	PSP_009758_2030_RED	0.25	Baldet Crater	
22	ESP_037082_1870_RED	0.25	S Arabia Terra	
23	ESP_018500_2000_RED	0.25	Crater NE of Jezero	
24	ESP_045307_2580_RED	0.25	Mare Boreum	
25	PSP_010413_1920_RED	0.25	Pettit Crater	
26	ESP_055318_2290_RED	0.25	Lyot Crater	
27	ESP_037201_2450_RED	0.25	Lomonosov Crater	
28	ESP_024237_1315_RED	0.25	Hellas Planitia	
29	ESP_022668_1340_RED	0.25	Hellas Planitia	
30	ESP_028410_1710_RED	0.50	Noctis Labyrinthus	
31	ESP_034274_1780_RED	0.25	Meridiani Planum	
32	PSP_001513_1655_RED	0.25	Gusev Crater	
33	ESP_025054_1370_RED	0.25	Hellas Planitia	
34	ESP_017610_1730_RED	0.25	Noctis Labyrinthus	
35	PSP_008097_1450_RED	0.50	Hellas Basin	
36	ESP_028856_1710_RED	0.25	Ganges Chasma	
37	ESP_022151_1660_RED	0.50	Crater West of Herschel	
38	PSP_002860_1650_RED	0.25	Herschel Crater	
39	ESP_035948_1900_RED	0.25	Arabia Terra	
40	ESP_043742_1800_RED	0.25	Meridiani Planum	
41	ESP_040058_1020_RED	0.25	Ultima Lingula	
42	ESP_062177_2370_RED	0.25	Kunowsky Crater	
43	ESP_062168_2585_RED	0.25	Mare Boreum	

44	ESP_063282_2225_RED	0.25	Renaudot Crater	
45	ESP_057799_1910_RED	0.25	Arabia Terra	
46	ESP_058788_1320_RED	0.25	Asimov Crater	
47	PSP_009721_2370_RED	0.25	Kunowsky Crater	
48	ESP_017426_2570_RED	0.25	Scandia Cavi	
49	ESP_018427_2640_RED	0.25	Mare Boreum	
50	ESP_061119_1990_RED	0.25	North of Jezero Crater	
51	PSP_005387_1935_RED	0.25	Ascraeus Mons	Lorenz et al. 2014
52	PSP_005032_1985_RED	0.25	Olympus Mons	Lorenz et al. 2014
53	PSP_006811_1910_RED	0.25	Ascraeus Mons	Lorenz et al. 2014
54	PSP_002249_1805_RED	0.25	Pavonis Mons	Lorenz et al. 2014
55	ESP_011928_2025_RED	0.25	NW of Olympus Mons	Lorenz et al. 2014
56	PSP_008460_1980_RED	0.25	Olympus Mons	Lorenz et al. 2014
57	PSP_005546_1960_RED	0.25	E of Olympus Mons	Lorenz et al. 2014
58	ESP_013655_1710_RED	0.25	Arsia Mons	Lorenz et al. 2014
59	PSP_005441_1970_RED	0.25	Olympus Mons	Lorenz et al. 2014
60	ESP_012310_1715_RED	0.25	Arsia Mons	Lorenz et al. 2014
61	PSP_002118_2015_RED	0.25	Olympus Mons	Lorenz et al. 2014
62	PSP_003476_1940_RED	0.25	Olympus Mons	Lorenz et al. 2014
63	PSP_001642_1895_RED	0.25	Ascraeus Mons	Lorenz et al. 2014
64	PSP_005783_1775_RED	0.25	Pavonis Mons	Lorenz et al. 2014
65	PSP_004754_1915_RED	0.25	Ascraeus Mons	Lorenz et al. 2014
66	PSP_004109_2010_RED	0.25	Olympus Mons	Lorenz et al. 2014
67	ESP_013998_2035_RED	0.25	Olympus Mons	Lorenz et al. 2014
68	PSP_005111_1985_RED	0.25	Olympus Mons	Lorenz et al. 2014
69	PSP_005084_1810_RED	0.25	Pavonis Mons	Lorenz et al. 2014
70	PSP_008341_1705_RED	0.25	Arsia Mons	Lorenz et al. 2014
71	PSP_010780_1805_RED	0.25	Pavonis Mons	Lorenz et al. 2014
72	PSP_010213_1785_RED	0.25	Pavonis Mons	Lorenz et al. 2014
73	PSP_005322_1955_RED	0.25	Olympus Mons	Lorenz et al. 2014
74	PSP_008803_1980_RED	0.25	Olympus Mons	Lorenz et al. 2014
75	ESP_014341_2035_RED	0.25	Olympus Mons	Lorenz et al. 2014

2. RIPPLE PATTERN MAPPING AND WAVELENGTH SURVEY

Different methods have been proposed to automatically map aeolian bedforms from HiRISE images. Previous studies mapped bedform crests, producing a set of polylines that can be used to assess bedform trends and lengths (Foroutan & Zimbelman, 2017; Vaz & Silvestro, 2014). These outputs can be used to study bedforms' spatial variations and patterns, however when applied at a dune field scale they generate a large set of crestlines, requiring subsequent spatial integration/generalization (Vaz et al., 2017). Furthermore, given the high number of ripples that can be present on one image, the size of the output

datasets may be of the same order of magnitude of the image itself (a few gigabits), which complicates the study of these bedforms at a global level.

Here we address these limitations by applying a new approach to Mars data for detection and quantification of bedform metrics, namely wavelength. We adapted the 2D Fast Fourier Transform (2D FFT) approach described by Voulgaris and Morin (2008) to study seabed bedforms, implementing a multiscale search scheme that allows the identification and characterization of large ripples and TARs (Transverse Aeolian Ridge) at different spatial scales. Figure S2 illustrates the adopted procedure.

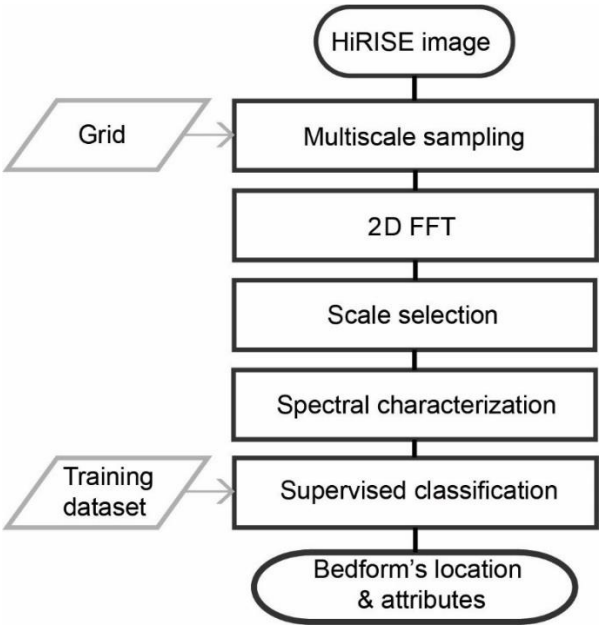

Fig. S2 - Flowchart with the main processing steps used to map and characterize large ripples and TARs using HiRISE images. See text for details.

Multiscale sampling

The technique we use to map the location of the bedforms and extract precise wavelength measurements begins with the creation of a regular grid which overlaps the HiRISE scene. A grid spacing of 15 m is used, so that we guarantee that each grid note includes several large ripples crests (~3 m spacing between crests). We then sample the image content around the grid nodes, with different spatial resolutions and window sizes (Fig. S3a). HiRISE images are stored in JP2000 image file format, therefore we take

advantage of the wavelet-based compression algorithm that is used in this format (Taubman & Marcellin, 2002) to sample the image at different scales (Fig. S3c-f). A dyadic sampling scheme is implemented, where the spatial resolution (r_s) at each scale/reduction level (L) is given as a function of the images' spatial resolution (r_i):

$$r_s = r_i * 2^L \qquad \text{(Eq. 1)}$$

This implies that the extent of the sampled area and the examined wavelength at each scale also increases proportionally to 2^L, while the dimensions of the sampled areas are constant. For instance, when L=0 the band-pass filter that is later applied in the spectral domain preserves wavelengths in the range 1-5 m, while when L=1 the range is 2-10 m (Fig. S3g-j). The only required input is the maximum wavelength of analysis, which is derived from a preliminary inspection of the image and that corresponds to the estimated maximum TAR spacing. This parameter is used to define the maximum L, controlling the maximum scale of analysis.

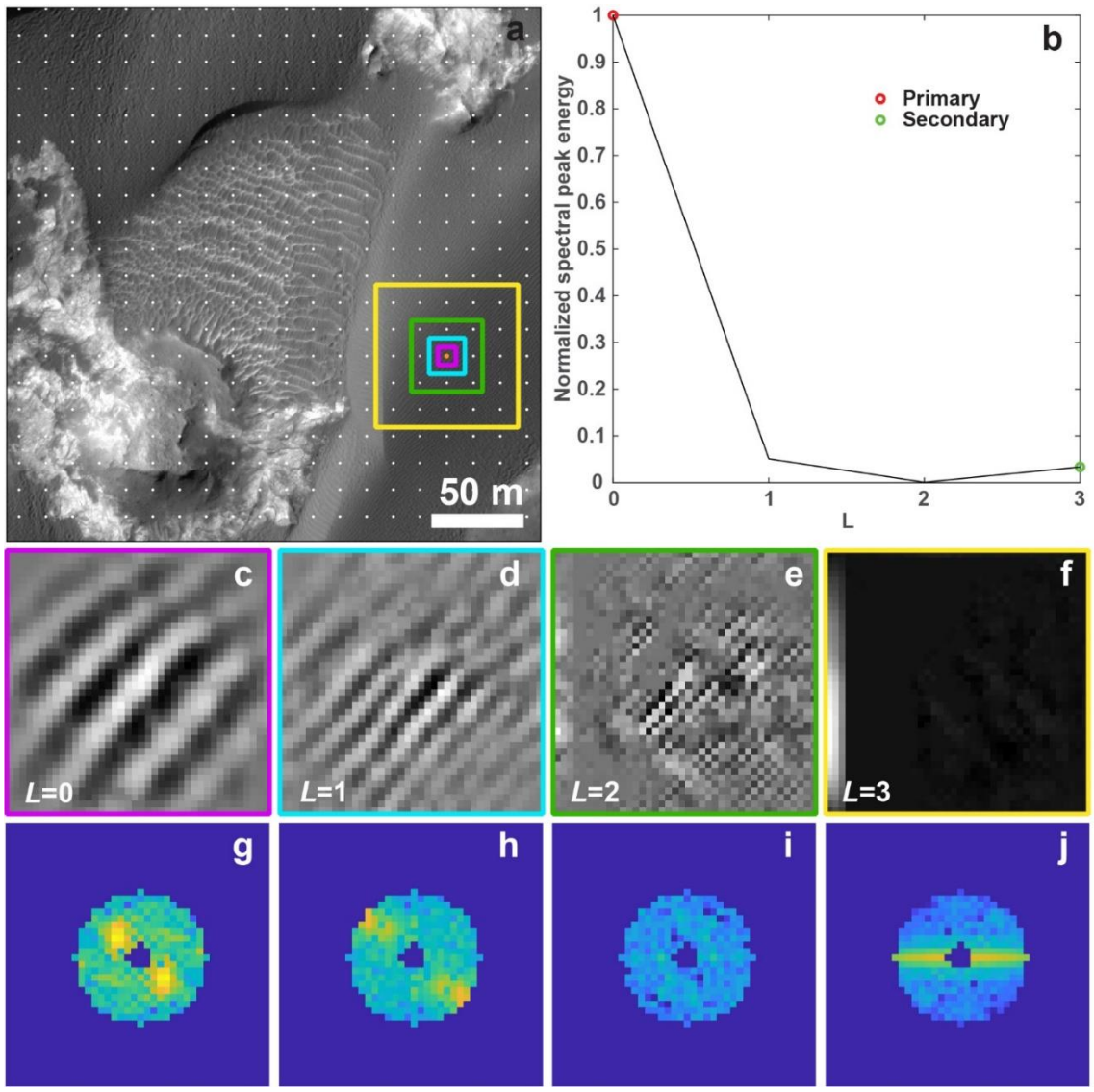

Fig. S3 – Example of the adopted sampling scheme and scale selection procedure (Area 2: ESP_018854_1755_RED). a) A grid with 15 m spacing is created and for each node the image is sampled at different spatial resolutions and extents (the colored outlines correspond to the extent of the sampled areas for each *L*, c-f). b) normalized peak energy (derived from g-j), the identification of the primary and secondary local maxima allows the selection of the best scales of analysis, i.e. the ones with more relevant and sharpest content. c-f) sampled datasets which include the filtering pre-processing described in the following section, note the smoother appearance of the corner areas created by the imposed circular taper function. Large ripples with straight crests are discernible when $0 \leq L \leq 2$, while for *L*=3 the albedo variation due to dune topography is the only recognizable feature. g-j) shifted 2D FFT spectra (values were stretched with a log transformation) for each *L*, a band pass filter is used to subset the target wavelengths at each scale. At *L=0* a strong peak is present, denoting the preferential trend and periodicity of the large ripples. The maximum energy at each scale is used to select the best scale/s of analysis (b).

2D FFT analysis and scale selection

The objective of the described sampling scheme is to implement the spectral characterization (which provides the characterization of the bedforms, for instance their trend and wavelength) in the most suitable scale of analysis, the same way as a mapper would use different zoom levels (i.e. different scales of analysis) to map ripples or larger TARs. To remove long wavelength components (e.g. created by dune topography) and increase the image contrast we subtract top-hat and bottom-hat (Soille, 2002) filtered versions of the input areas (a circular structuring element with radius 8 is used). To reduce the artifacts caused by the non-isotropic sampling (the sampled areas have square shapes) we multiply the matrix by a circular taper function (computed as the normalized Euclidean distance to the central pixel). Figures S3c-f show the results of these operations, which prepare the data for the subsequent spectral analysis.

A 2D spectrum is computed for each filtered area/scale using the FFT. A band-pass filter is applied in the spectral domain, which subsets the analyzed wavelength range on each scale. The same scaling function described in Eq. 1 is used to define the target wavelength ranges, starting at a range of 1-5 m for L=0 (Fig. S3g-j). Power spectrums (the square of the transform magnitudes; Gonzalez et al., 2004) are computed and the spectral peak energies (S_L) are collected for each scale (Voulgaris & Morin, 2008). This is the parameter used to choose the most relevant scale (i.e. the scale with the sharpest periodic features), which is found by identifying the local maxima of the peak spectral energy across scales (Fig. S3b). In certain situations, different sets of bedforms with different trends and wavelengths overlap in the same areas, which translates in the existence of a secondary maxima. If present, the two local maxima are recorded, while if only one is present the secondary scale is set as $argmax(S_L)$-1. No secondary maxima is derived when $argmax(S_L)$ is one.

Spectral and textural characterization

The objective of this processing step is twofold: 1) measure the trend and wavelength of the bedforms, and 2) assemble a sparse set of descriptors that summarize image proprieties and textures, to be used in the following classification step. Table S1 lists the computed parameters and detail how they were computed while Fig. S4 show some examples. The same descriptors are computed for the two selected scales and stored in a

database. We adopted the same approach described by Voulgaris and Morin (2008) to measure the wavelength and the trend of the bedforms. Additionally, we apply a kernel-based technique to analyze the circular distribution derived from the spectral analysis in order to parameterize bimodal circular distributions (Vaz et al., 2015), which is of relevance since the trend of large ripples may not be unidirectional.

Table S2 – List of parameters compiled for the identified primary and secondary scales.

Description	Descriptors	Details	References
Selected scale/reduction level	*L* (Fig. S4b)	See previous section for details	
Normalized peak energy	S_L	e.g., Fig. S3b	
Azimuth	Trend of the spectral peak	Sub-pixel interpolation using the neighborhood of the maximum peak	(Voulgaris & Morin, 2008)
Wavelength	Wavelength of the spectral peak (Fig. S4e)	Sub-pixel interpolation using the neighborhood of the maximum peak	(Voulgaris & Morin, 2008)
Average trend and wavelength	Mean vector trend, circular standard deviation (Fig. S4d), circular skewness and kurtosis. Wavelength weighted average and standard deviation.	Spectral energies are used as weighting factor.	
Directional modes	Trend of the primary and secondary modes. Primary mode kernel frequency (Fig. S4f) and kernel frequency ratio.	Spectral energies are used as weighting factor and a kernel window of 20º is used to create the circular kernel function (see Vaz et al., 2015 for details).	(Vaz et al., 2015)
Spectral proprieties	Maximum peak energy. Peak and quality indices (Fig. S4c).	Provide textural context and can be regarded as proxies for bedform/image sharpness	(Voulgaris & Morin, 2008)
Lambert albedo	Lambert albedo (I/F) average and standard deviation	Computed using the scaling factors and offsets obtained from the HiRISE label files	

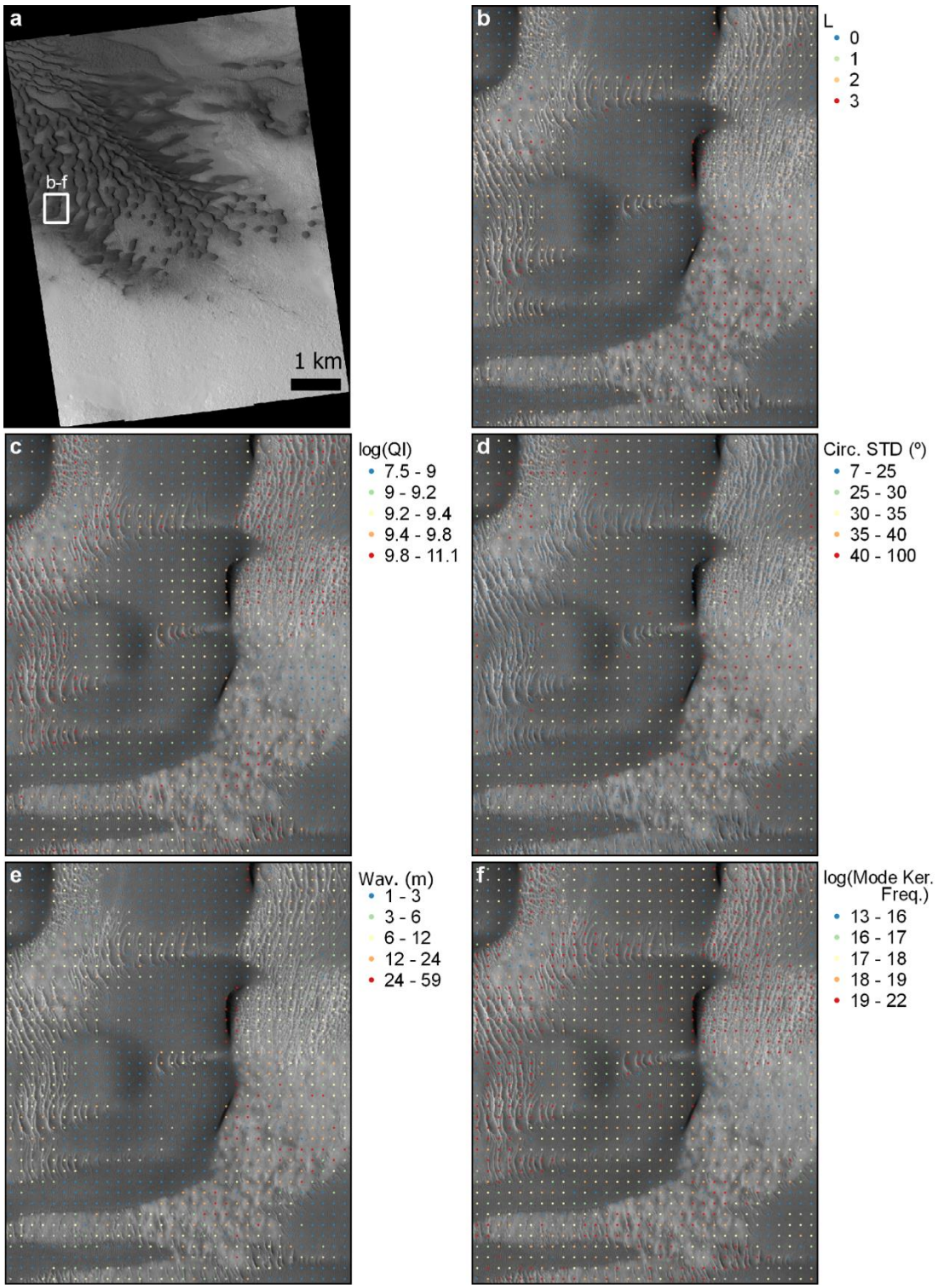

Fig. S4 – Examples of pattern descriptors used in the classification process (see Table S2 for details and Fig. S5 for the classification outputs). a) HiRISE image (Area 1: ESP_027864_2295_RED). b) Selected primary scale. c) Quality index (stretched using a log scaling). d) Circular standard deviation. e) Spectral peak wavelength. f) Kernel frequency of the main mode (stretched using a log scaling).

Supervised classification

Bedforms are typically scattered covering different types of surfaces (e.g. bedrock, regolith), and do not usually form a continuous patch. Therefore, we need to discriminate two classes: targeted bedforms (large ripples, megaripples and TARs) and bedrock (including slipfaces and other long-wavelength or shadowed terrains). To achieve this, we implemented a supervised classification using artificial neural networks (ANN). We use a feedforward ANN architecture with one input, one hidden (38 nodes) and one output layer (two nodes). We use hyperbolic tangent transfer functions and conjugate gradient backpropagation (Moller, 1993) to train the networks.

All the fields listed in Table S2 that correspond to azimuthal information are excluded from the classification procedure (using them would result in directional bias). The remaining parameters for the primary and secondary scales are normalized (min-max normalization) to serve as inputs to the ANN classifier. The training datasets were digitized for each area using QGIS and a random partition (train, test, and validation datasets) is performed. Fig. S5 show examples of training data and output final classification.

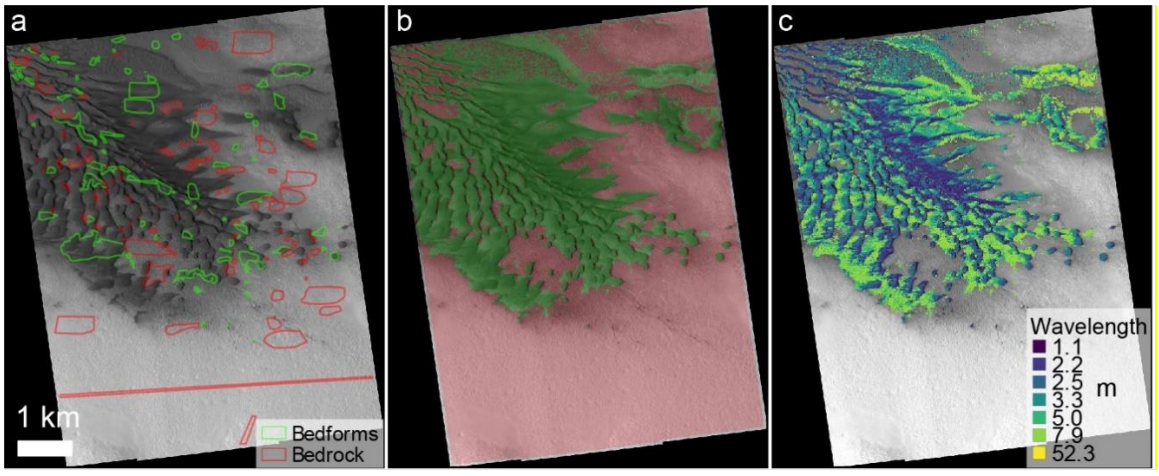

Fig. S5 - Classification process overview. a) Labeled training data (Area 1: ESP_027864_2295_RED). b) Output classification (accuracy of 96.6%). c) Measured bedform wavelength.

Accuracy Assessment

To assess the performance of the described technique we need to evaluate two types of accuracies: 1) classification accuracy: how well can we identify and map bedforms?; and 2) wavelength accuracy: can we retrieve accurate wavelength measurements?

178 The first question is addressed by creating confusion matrices and computing the
179 overall accuracy and kappa index to evaluate the classification results. Overall, the training
180 data corresponds to 7.5% of total mapped area, with a prevalence (percentage of bedform
181 class in the training dataset) of 59%. The overall classification accuracy is 93.7% (kappa
182 index of 0.87) which demonstrates the excellent performance of the proposed technique
183 (Table S3).
184
185 **Table S3 – Accuracy of the supervised classification with two classes: bedforms (large ripples and**
186 **TARs) and bedrock (other non-bedforms features). Overall accuracy ranges from 0 to 100%, with**
187 **100% denoting a perfect classification. Kappa index range from 0 to 1, where 0 corresponds to a**
188 **random non-agreement case. Prevalence is the percentage of training data that correspond to the**
189 **positive case (bedform class), ideally if should be ~50%. N is the number of mapped grid nodes. The**
190 **training dataset corresponds to 7.5% of the total mapped area.**
191

Area ID	Accuracy (%)	Kappa index	Prevalence (%)	N	Train %
1	96.6	0.93	58.1	20923	10.0
2	98.0	0.87	90.7	56423	15.9
3	97.8	0.93	19.6	19659	7.3
4	92.5	0.83	66.2	28902	14.6
5	92.3	0.84	63.8	39844	10.7
6	88.0	0.73	68.6	29173	17.3
7	94.3	0.86	28.1	14635	3.7
8	96.1	0.91	66.3	60308	20.0
9	93.4	0.81	79.6	52435	16.7
10	96.0	0.91	68.5	9534	2.6
11	93.4	0.87	47.5	21168	6.8
12	94.1	0.86	71.4	16189	3.0
13	94.5	0.87	30.8	6779	5.8
14	90.2	0.80	50.7	13724	14.2
15	94.7	0.87	29.0	15132	5.1
16	92.9	0.85	60.1	11059	5.2
17	99.2	0.95	91.4	29229	13.2
18	91.3	0.81	37.1	31141	11.6
19	94.8	0.90	44.6	31954	15.5
20	90.2	0.80	43.3	46403	22.8
21	95.0	0.84	17.0	17445	3.3
22	88.7	0.76	33.0	14769	8.5
23	98.0	0.96	46.2	19334	6.1
24	96.1	0.92	63.7	23035	5.7
25	94.8	0.88	67.0	39433	9.7
26	98.1	0.96	66.5	22238	9.5
27	94.8	0.89	57.4	8663	1.7

28	94.4	0.89	44.3	11122	5.2
29	89.9	0.70	17.4	15666	7.6
30	94.1	0.52	91.8	45895	6.0
31	97.0	0.94	45.5	13917	3.9
32	92.3	0.72	81.5	28053	5.2
33	87.8	0.75	54.9	27698	8.5
34	95.3	0.89	71.0	13885	6.0
35	85.3	0.71	47.6	77548	12.9
36	92.6	0.76	83.1	15699	7.0
37	93.5	0.87	45.7	13657	12.0
38	90.4	0.80	35.9	11340	3.2
39	95.3	0.91	47.0	23407	8.4
40	97.3	0.95	53.2	38685	14.1
41	94.6	0.88	67.4	4484	3.0
42	92.1	0.84	55.3	18859	7.8
43	98.7	0.96	18.5	14804	7.1
44	93.1	0.83	27.2	17261	9.8
45	96.5	0.90	78.6	19742	16.3
46	93.3	0.75	86.4	31039	11.6
47	92.0	0.82	65.4	31130	7.8
48	93.9	0.87	37.1	43224	11.8
49	94.5	0.88	64.4	52921	7.3
50	95.2	0.90	64.4	20660	9.2
51	91.8	0.72	81.2	32572	6.8
52	96.4	0.8	12.9	4926	1.4
53	90.4	0.8	34.8	11924	4.3
54	96.2	0.9	17.2	4521	3.6
55	93.7	0.7	84.4	14067	6.6
56	99.5	0.8	1.4	13800	5.8
57	90.3	0.8	59.2	41672	10.4
58	98.9	1.0	16.4	28720	26.1
59	90.6	0.8	70.4	15438	3.3
60	97.7	0.9	81.0	25090	6.8
61	90.5	0.8	70.8	16495	6.1
62	89.4	0.8	67.3	11844	2.5
63	97.8	0.9	27.9	10764	3.1
64	98.0	0.9	17.0	5810	3.4
65	90.8	0.8	38.0	36124	10.8
66	98.2	1.0	36.6	5438	2.1
67	92.6	0.5	92.8	49404	15.9
68	89.1	0.8	56.1	5046	0.9
69	99.1	1.0	75.5	21921	4.4
70	98.0	0.9	15.1	11501	5.4
71	99.3	0.7	1.2	8536	2.9

72	96.7	0.8	10.0	3379	1.4
73	97.6	0.8	90.9	32621	8.1
74	91.1	0.7	19.4	18819	3.7
75	93.4	0.8	77.7	46119	10.9
Total	93.71	0.87	58.8	1766778	7.45

To evaluate the accuracy of the wavelength measurements we use hillshade images of synthetic bedforms' topography, modelled with a superellipse function (Eq. 2). Transverse bedform topography is modelled with n=0.4 and h= λ /10 (h represents the maximum height of the bedforms and corresponds to 1/10 of the wavelength λ). The length of the bedforms is assumed to scale with wavelength (λ*50) and is controlled with a longitudinal taper, obtained with n=4 and h=1.

$$|\boldsymbol{x}|^{\boldsymbol{n}} + \left|\frac{\boldsymbol{y}}{\boldsymbol{h}}\right|^{\boldsymbol{n}} = \mathbf{1} \qquad \text{(Eq. 2)}$$

Random azimuths allow to test the directional precision of the adopted technique. Fig. S6a-c shows examples of the test datasets, displaying periodic bedform-like features with different trend and spacing. In Fig. S6d we evaluate our measurements (peak and average) for a wide range of wavelengths. Peak wavelengths provide the most accurate predictions (average error of 3% and trend accuracy below 1º, Table S4) and present narrower uncertainty bars. Additionally, we demonstrate the stability of the sampling and scale selection schemes, with a regular progression of L with increasing wavelength (Fig. S6d).

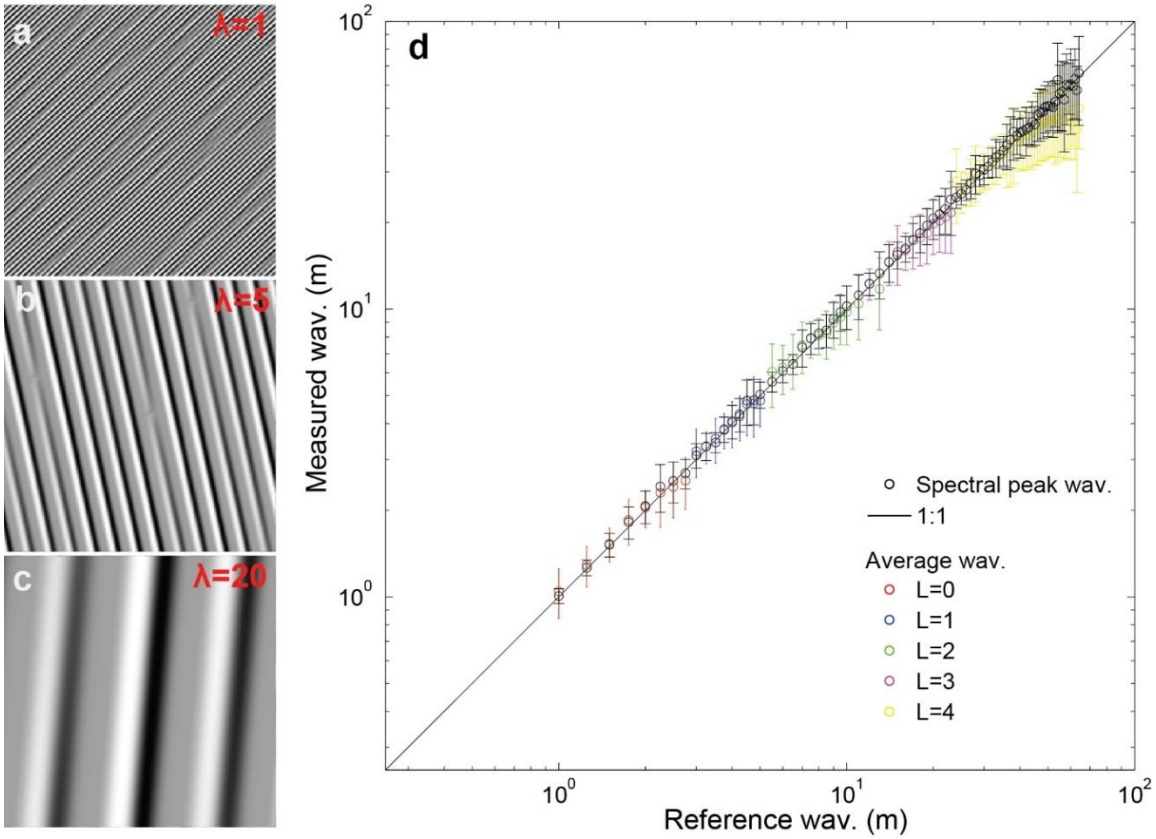

Fig. S6 – Wavelength accuracy assessment using synthetic hillshade views of periodic bedform-like patterns. a-c) Examples of the datasets created using random trends (λ corresponds to the crest spacing in meters). d) Measured vs. modelled wavelength, the black line corresponds to a perfect agreement case while two different wavelength estimates are shown: the spectral peak wavelength which produces more accurate results across all scales of analysis and with smaller uncertainty bars, and the average wavelength with larger uncertainty bars. The different scales of analysis (*L*) are depicted in different colors, note the congruent sequency of selected scales when wavelength increases.

Table S4 – Wavelength percentual error and azimuth error computed using synthetic datasets (Fig. S6). We estimate wavelength errors of 3% and trend errors of less than 1º.

Measurement type	Wavelength percent error (average±STD %)	Azimuth error (average ±STD º)
Spectral peak	2.7±2.3	-0.1±0.8
Spectral average	6.4±6.9	-0.01±0.6

Finally, a total of 978 reference wavelength measurements were compiled in QGIS (e.g. Fig. S7a) and compared with our results. Fig. S7b highlights the linear response of the mapping algorithm for a large range of values. We compute an average percentual difference of -0.7±11.9% (Table S5), which demonstrates that the obtained results are not

biased and that differences are within a standard deviation interval of ±12%. Besides this detailed local assessment, section 4 presents a global comparison with previously published measurements.

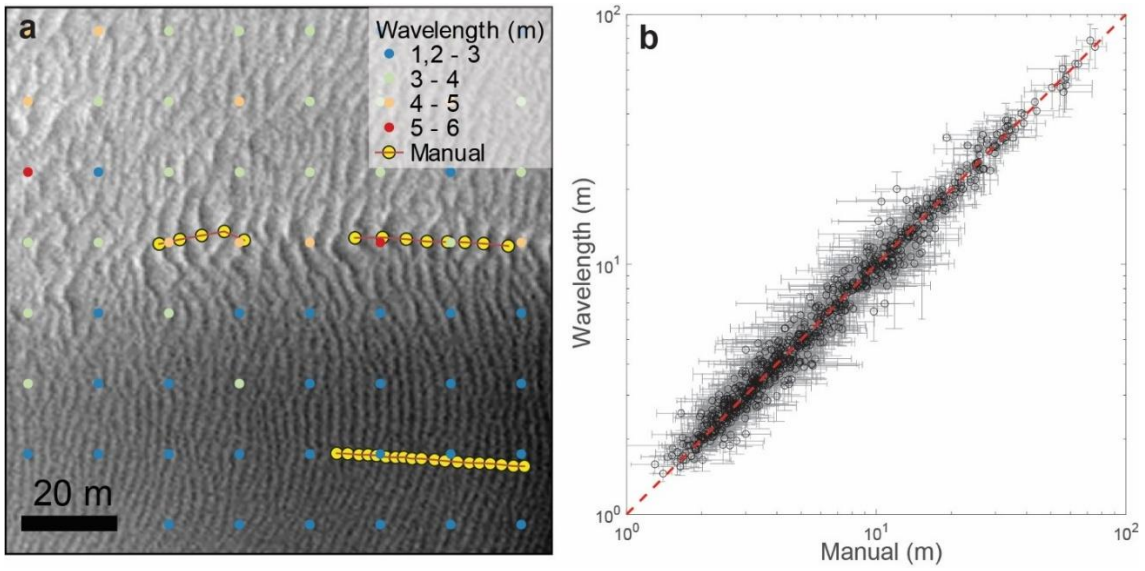

Fig. S7 – Comparison of wavelength measurements. a) Example of reference wavelength measurements obtained by mapping successive bedform crests (yellow dots), the peak wavelength obtained automatically is also shown. b) automated wavelength estimates vs. manually derived measurements (manual estimates were averaged and integrated into the sampling grid using a 7.5 m spatial buffer), the red line corresponds to a 1:1 ratio.

Table S5 – Wavelength was compared for five different areas, including one with coarser spatial resolution. Overall, we estimate that the obtained wavelengths are comparable to manually derived measurements within a ±12% confidence interval.

Area ID	Percent difference (average±STD %)	N	Spatial resolution (m/pix)
1	-0.8±11.6	331	0.25
2	-1.7±14.4	181	0.25
3	-0.6±12.5	192	0.25
4	0.7±9	111	0.25
8	-0.1±10.1	163	0.5
All	-0.7±11.9	978	

3. BEDFORM POPULATION SEGMENTATION AND SUMMARY STATISTICS

Two main characteristics are commonly used to discriminate and classify Martian aeolian bedforms from remote sensing imagery: wavelength and albedo (Day & Zimbelman, 2021). We use an exploratory and iterative approach to set threshold values for these two parameters. This allows a quantitative and more objective segmentation of the bedform types. To the purpose of this work, we discriminate two classes: large ripples and megaripples & TARs. We create 2D kernel density histograms using the mapped bedform's wavelength (e.g. Fig. S5c), HiRISE Lambertian albedo (I/F) and circular standard deviation (here used as a proxy to crest straightness). These plots are inspected for each area, and putative wavelength and albedo thresholds are selected (Fig. S8e, f). These values are then tested/visualized in QGIS and iteratively adjusted (Fig. S8b-d). In most cases this is a straightforward process, since large ripples cover extensive areas, thus forming clear maxima corresponding to meter-scale wavelengths and low albedos. Fig. S8 shows how the threshold values identified in the histograms correspond to clear pattern changes in map view. Supporting information S2 includes the histograms and global map views for all the mapped areas.

In this work we focus on a first order segmentation, collapsing the data into two classes. Yet, in some areas the plots also highlight the presence of second order sub-populations, which may be attributed to the effect of dune topography and/or granulometric differences (for instance between putative megaripples and TARs, Fig. S9). A finer analysis and clustering are thus possible, although it is out of the scope of this paper.

Summary statistics (wavelength mean and standard deviation) are computed for the two classes and constitute the basis of the following analysis. To help to identify outliers and evaluate possible relations between dune morphology and large ripples morphometry, we identified the type of dunes in the areas mapped outside Tharsis (Fig. S15), as that region lacks dark dunes. Most areas present more than one dune type, therefore we used a dual classification scheme, visually identifying a primary and secondary dune types. Primary class corresponds to the type of dune most abundant, in terms of relative area.

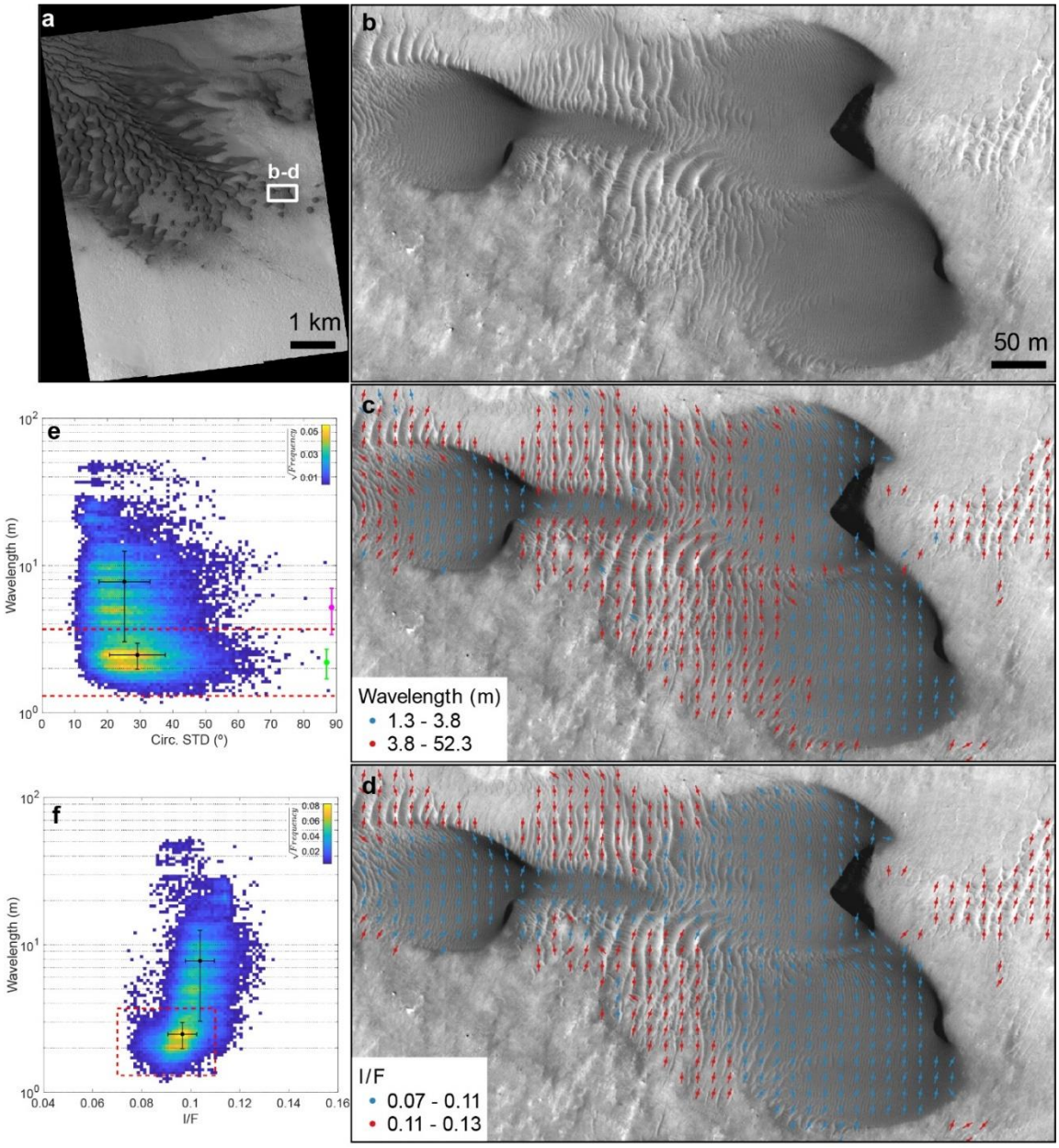

Fig. S8 – Bedform segmentation using wavelength and albedo threshold values derived from 2D histograms. a, b) HiRISE image (Area 1: ESP_027864_2295_RED). c) map view of the two classes defined using a wavelength threshold range of 1.3-3.8 m (large ripples) and >3.8 m (megaripples & TARs); these values correspond to the red dashed lines in (e); the trend of the mapped bedforms is also shown. d) map view of the two classes defined using an albedo threshold range of 0.07-0.11 (large ripples) and >0.11 (megaripples & TARs); these values correspond to the vertical red dashed lines in (f); the trend of the mapped bedforms is also shown. e) 2D histogram relating bedforms' wavelength and circular standard deviation (to improve readability the frequencies were scaled with a square root function), the defined threshold values are depicted as red dashed lines (figure (c) provides a map view), note the main maxima corresponding to a wavelength of ~2.5 m; the black dots and variation intervals correspond to the averages and standard deviations computed for the segmented classes; the green (large ripples) and magenta (TARs) dots located near the right edge of the plot correspond to the summary statistics of Lapotre et al. (2016). f) 2D histogram relating bedforms' wavelength and albedo (frequencies were scaled with a square root function), the defined threshold values are depicted

as a red square (figures (c, d) provide map views of the two parameters); the black dots and intervals correspond to the computed averages and standard deviations.

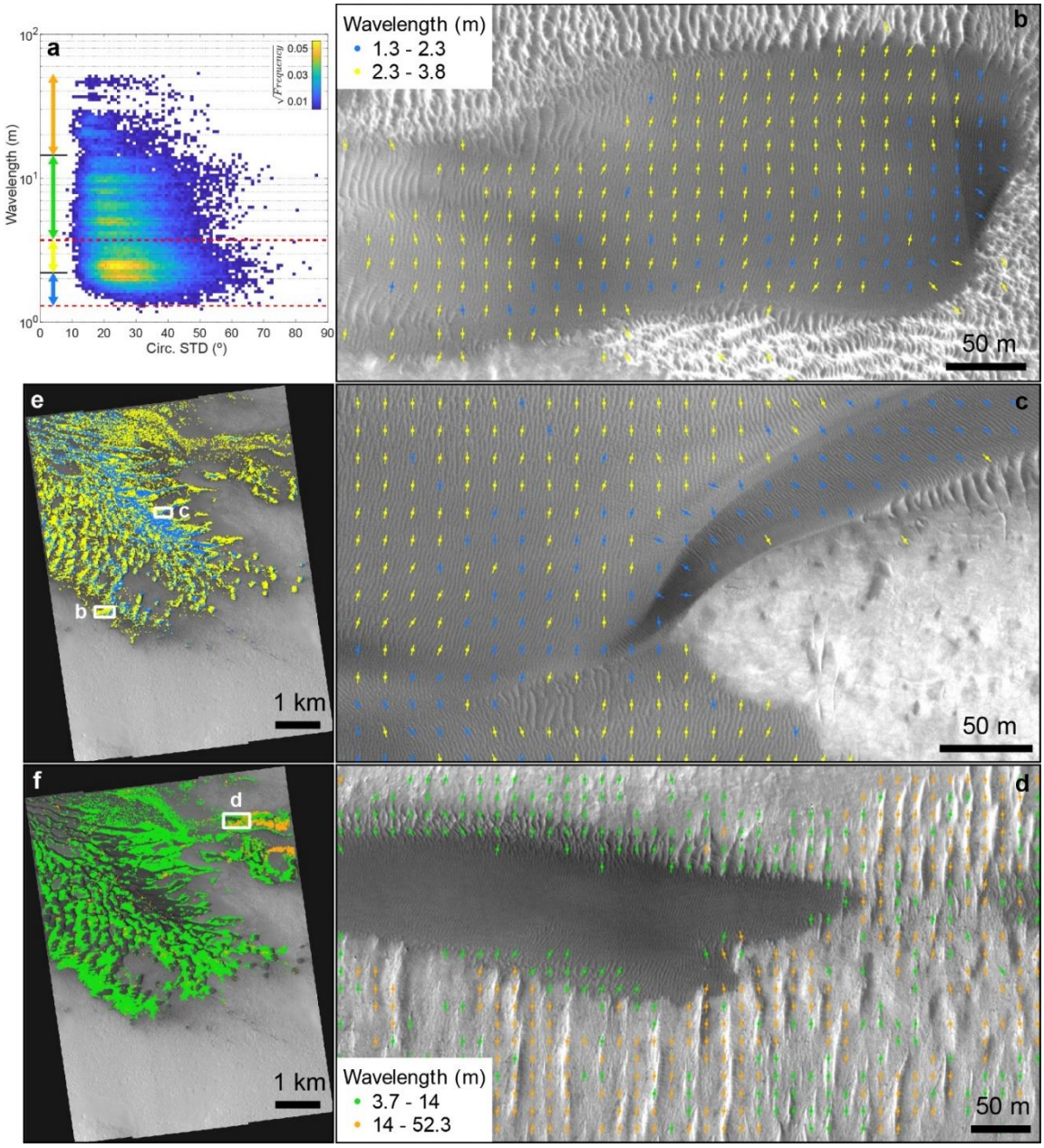

Fig. S9 - To establish direct comparisons with previous studies only a first order bedform segmentation is discussed in this work (Fig. S8), nevertheless this example illustrates the possibility to pursuit more detailed studies in the future. a) 2D histogram showing the wavelength intervals that produce the partition shown in the map views, the first order wavelength thresholds correspond to the red dashed lines while the colored double arrows identify the wavelength intervals shown in the map views. b, c, e) possible secondary partition of the large meter-scale ripples, bedforms with less than 2.3 m appear clustered in the center of the dune field (e) and occur in the downwind sections of some dunes (b, c). d, f) possible megaripples are widespread (f), have wavelengths between 3.7 and 14 m, are located in the

lower sections of the dunes and appear in continuity with large ripples (d), while TARs have larger wavelengths and are mainly located in the NE corner of the mapped area (f).

4. COMPARISON WITH PUBLISHED MEASUREMENTS

In this section we compare our results with the ones obtained by Lapotre et al. (2016) and Lorenz et al. (2014) for a total of 11 and 25 areas, respectively (Table S6). The average large ripples wavelengths computed in this study are inline with the values reported by Lapotre et al. (2016) (Fig. S10a). On average, we estimate a percentual difference of 4±10% with a maximum difference of 21% for Area 2 (Table S6). If we also consider the standard deviation intervals, we conclude that the two sets of measurements are very similar, presenting overlapping distributions (Fig. S10a and Table S6). The case of the larger bedforms seems to be different, with an average percentual difference of 84±83% and a maximum of 236%. Even if we have overlapping distributions in four areas (Fig. S10b, note how in some cases the standard deviation intervals intersect the 1:1 line), half of Lapotre et al. (2016) areas clearly show an underestimation of the larger bedforms' wavelengths (data points and standard deviations below the 1:1 curve, Fig. S10b).

In summary, our wavelength estimates for the large ripples are consistent with the measurements made by Lapotre et al. (2016). We found that for most of the areas the averages differ by less than 10%, approximately the same confidence interval derived from the comparison made with manually derived measurements in this work (±12% confidence interval, Table S5). To understand the larger discrepancies associated with the larger bedforms, one must question if the sampling used by Lapotre et al. (2016) was enough to characterize these populations. Focusing in the two areas with larger differences (Areas 6 and 8), Lapotre et al. (2016) collected 36 and 40 measurements for TARs and 136 and 98 for large ripples. These were randomly sampled across the HiRISE scenes. Yet, our complete mapping reveals that TARs only cover a small fraction of the mapped areas (38 and 20% respectively), in addition TARs tend to form disperse sets of bedforms with variable wavelengths. Therefore, we hypothesize that a more complete sampling would be needed to characterize these populations and that this is the main reason for the observed wavelength disparities.

Lorenz et al. (2014) values are consistently underestimated when compare with our measurements (Fig. S10a). On average, their values differ by 73±106% with a maximum

percentual difference of 563% (Area 55, Table S6). In this specific area, Lorenz et al. (2014) reported an average wavelength of 0.5 m, which is a questionable estimate since it only corresponds to two pixels. This was noted in Lapotre et al. (2021), which replace this value by an estimated wavelength of ~1 m (see their Fig. 2). In each area Lorenz et al. (2014) sampled approximately 40 sets of bedforms, divided by four selected sub-areas. Among other possible causes (e.g. non-random sampling), also in this case we hypothesize that under sampling may have contributed to the measured differences. Bedforms in the Tharsis region do not form unambiguous dune fields or sand sheets, and most of the times they are scattered or preferentially located in depressions. This non-uniform spatial distribution may further complicate the obtention of representative wavelength samples from a few tens of measurements. In section 5 we argue that Tharsis bedforms represent a different type of bedforms and that merging the two datasets is not appropriate. In any case, from the validation presented in section 2 and from the comparison with Lapotre et al. (2016) results we determine that wavelengths derived with our method are robust, which means Lorenz et al. (2014) results denote a systematic underestimation (Fig. S11a).

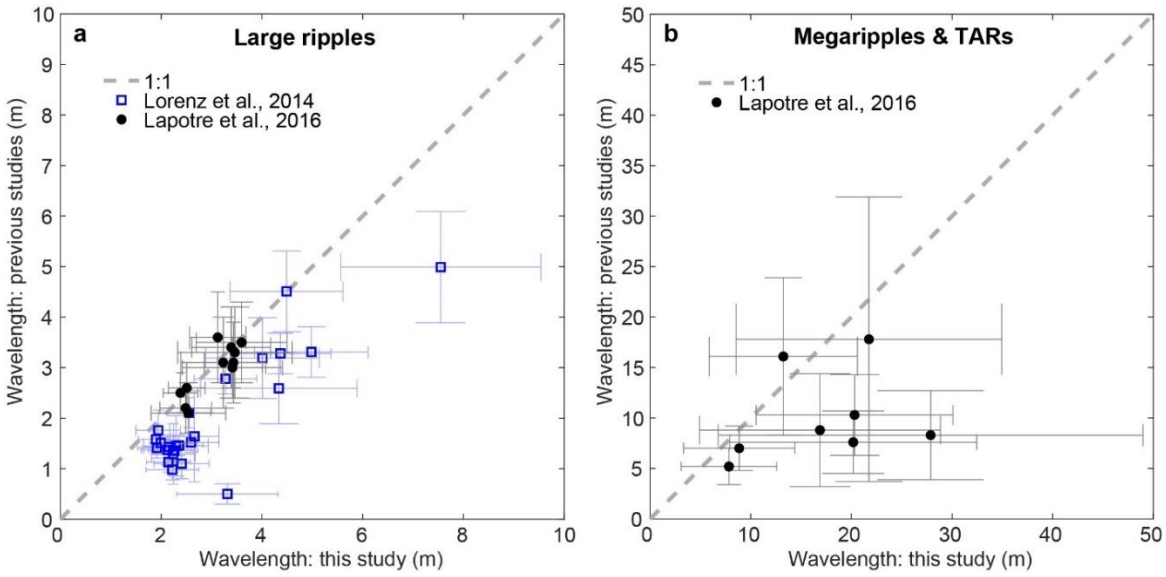

Fig. S10 – Comparison of wavelength measurements. a) Large ripples, there is a good agreement with Lapotre et al. (2016) values and error bars always overlap the 1:1 (perfect agreement) line; when compared with our data, Lorenz et al. (2014) measurements are clearly underestimated. b) In the case of the larger bedforms, half of Lapotre et al. (2016) values are comparable to our data, while the other half seems to be relatively underestimated.

Previous works used MOLA elevations to compute atmospheric density, so this is also a variable we try to verify and compare. The elevations presented in this work are automatically extracted from the MOLA MEGDR (Mission Experiment Gridded Data Records), which represent elevations above the areoid with a spatial resolution of 463 m/pixel (Smith et al., 1999). The spatial centroids of the largest bedform patches mapped in each area are used as sampling points. Lorenz et al. (2014) mentions that their elevation data was derived from MOLA data, however they do not provide any other detail (e.g. specific sampling locations, reference datum or methods used to collect the elevation values). In their supplementary materials, Lapotre et al. (2016) mentions that Lorenz's data "were measured with respect to the Mars Reconnaissance Orbiter reference ellipsoid" and that for this reasons they have corrected the data to be consistent with the areoid datum used in their survey. We applied the same correction, converting Lorenz's (2014) elevations to orthographic heights.

We found a good agreement with Lapotre et al. (2016) elevations (Fig. S11b), the only exception is Area 3, which has an elevation difference of ~700 m. In this specific case, elevations inside the mapped area can vary by ~ 1000 m, therefore the mentioned discrepancy can be attributed to the different sampling location.

We found significant differences between the elevations computed in this work and part of the elevations reported in Lorenz et al. (2014). In four areas differences can range between 2 and 3 km (Fig. S11b). Also in this case, differences are likely caused by a different sampling location. The Tharsis region extreme topography result in large elevation variations across the HiRISE image footprints. In some cases, maximum elevation differences of ~4 km are possible, depending where in the image footprint the MOLA data is sampled.

We conclude that relevant elevation differences may exist between studies. These are due to the uncertain location of the sampling points and produce higher disparities for the studied areas located in the Tharsis region. We implicitly use the location of the mapped bedforms to define the sampling points, thus we adopt a more consistent and robust methodology which reduces the uncertainty in the measurement of this variable.

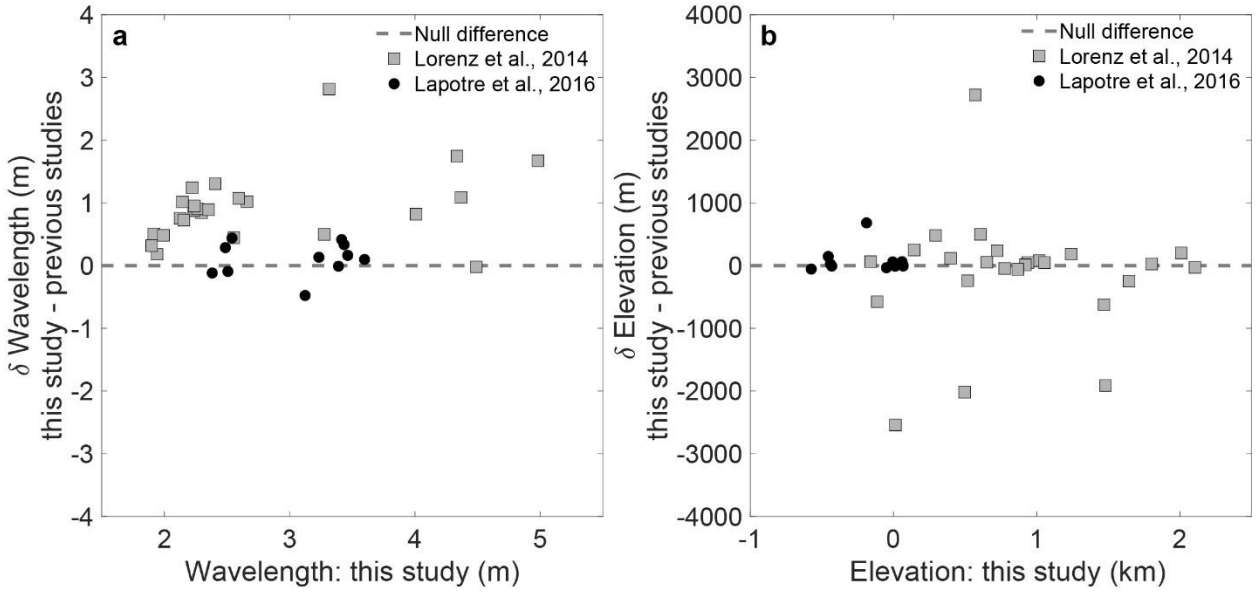

Fig. S11 – Differences in large ripples' average wavelength and elevation. a) Wavelength differences between our measurements and Lapotre et al. (2016) are small and cluster around 0 m, while Lorenz et al. (2014) dataset presents higher discrepancies and are consistently bellow the values obtained in this study. b) Lapotre et al. (2016) elevation values are consistent with our work, except for Area 3 which has an elevation difference of ~700 m, yet this is understandable since inside the mapped area elevations can vary by ~ 1000 m; the differences with Lorenz et al. (2014) measurements are more relevant, with elevation differences that can reach 3 km, which is justified by the fact that high slope areas in the Tharsis region (e.g. Olympus Mons basal scarp) can produce large topographic differences (we measured elevation ranges up to 4 km) even inside the relatively small footprint of an HiRISE image.

Table S6 – Comparison of wavelength summary statistics, the first 11 areas correspond to the areas analyzed by Lapotre et al. (2016) while area IDs above 51 correspond to the 25 areas studied in Lorenz et al. (2014). Summary statistics (average and standard deviation) are reported, and percentual errors were computed according to: 100*($Wav_{this\ study}$ − $Wav_{other\ studies}$) / $Wav_{other\ studies}$.

	Large ripples		TARs & megaripples		Percentual differences	
Area ID	Wav. avg. ± STD (m)	Wav. avg. ± STD (Lapotre, 2016 / Lorenz, 2014)	Wav. avg. ± STD (m)	Wav. avg. ± STD (Lapotre, 2016 / Lorenz, 2014)	LRs % difference	TARs % difference
1	2.5 ± 0.5	2.2 ± 0.5	7.8 ± 4.8	5.2 ± 1.8	13.0	50.7
2	2.5 ± 0.7	2.1 ± 0.6	8.9 ± 5.5	7 ± 2.2	20.9	26.5
3	3.4 ± 1	3 ± 0.6	13.2 ± 7.4	16.1 ± 7.8	13.8	-17.8
4	3.6 ± 0.9	3.5 ± 0.8	16.9 ± 12	8.8 ± 5.6	2.8	91.8
5	3.5 ± 1.1	3.3 ± 0.9	21.7 ± 13.2	17.8 ± 14.1	5.0	22.2
6	3.2 ± 0.8	3.1 ± 0.9	20.2 ± 12.3	7.6 ± 3.1	4.3	165.6
7	3.4 ± 0.6	3.1 ± 0.8	20.3 ± 9.8	10.3 ± 4	10.8	97.3
8	3.1 ± 0.6	3.6 ± 0.9	27.9 ± 21.1	8.3 ± 4.4	-13.2	235.8
9	2.5 ± 0.4	2.6 ± 0.5	7.4 ± 4.1		-3.6	
10	2.4 ± 0.3	2.5 ± 0.4	9.6 ± 7		-4.7	

11	3.4 ± 0.8	3.4 ± 0.8	13 ± 7.7	-0.3
51	2.7 ± 0.5	1.6 ± 0.9	7.4 ± 4.7	62.1
52	5 ± 1.1	3.3 ± 0.5		50.5
53	4.4 ± 1	3.3 ± 0.4	13.1 ± 9.9	33.1
54	2.6 ± 0.4	2.1 ± 0.3	6 ± 1.2	21.0
55	3.3 ± 1	0.5 ± 0.2	12.4 ± 5.7	563.0
56	7.5 ± 2	5 ± 1.1	17.8 ± 2.1	51.3
57	2.3 ± 0.6	1.5 ± 0.6	16.3 ± 14	58.3
58	2.2 ± 0.5	1.4 ± 0.2	7.6 ± 4	64.3
59	2.1 ± 0.4	1.1 ± 0.2	5.1 ± 3.7	89.7
60	1.9 ± 0.4	1.4 ± 0.2	5.6 ± 1.1	35.8
61	2.3 ± 0.5	1.4 ± 0.2	5 ± 1.3	66.5
62	2.2 ± 0.4	1.3 ± 0.6	4.1 ± 0.9	73.7
63	2.6 ± 0.5	1.5 ± 0.2	19.2 ± 13.4	70.6
64	1.9 ± 0.4	1.8 ± 0.4	24.4 ± 10	10.3
65	4 ± 1.1	3.2 ± 0.8	14.6 ± 7.5	25.7
66	2.4 ± 0.5	1.5 ± 0.2	4.3 ± 0.6	61.1
67	2.4 ± 0.5	1.1 ± 0.3	6.6 ± 4.2	118.7
68	4.3 ± 1.6	2.6 ± 0.7	10.5 ± 1.2	67.4
69	1.9 ± 0.4	1.6 ± 0.3	14.1 ± 3.9	20.1
70	4.5 ± 1.1	4.5 ± 0.8	21 ± 14	-0.5
71	3.3 ± 0.6	2.8 ± 0.3	8.7 ± 1.8	17.9
72	2 ± 0.2	1.5 ± 0.1	20.7 ± 11.7	32.0
73	2.2 ± 0.5	1 ± 0.2	5.9 ± 1.7	126.7
74	2.1 ± 0.5	1.4 ± 0.3	14 ± 10.6	55.2
75	2.2 ± 0.5	1.4 ± 0.2	8.7 ± 3.8	50.7

5. EXPLORATORY DATA ANALYSIS AND OUTLIER IDENTIFICATION

We note that Lapotre et al. (2016) merged their dataset with the one derived by Lorenz et al. (2014), and evaluated the model predictions using both datasets. In contrast, a segmentation of the two datasets and the fit of different models was later preferred (Lapotre et al., 2021; Lorenz, 2020). Therefore, the first question we address here is: can we integrate the measurements made in the Tharsis region with others made elsewhere on Mars, or do they constitute different sets of bedforms? To answer this question, we evaluate if there is a unique and continuous distribution of wavelength and albedo. Then we briefly discuss the morphological differences and overall setting and significance of the two sets of bedforms.

In Fig. S12 we compare the wavelength and albedo distributions of the large ripples mapped in the Tharsis region (the same 25 areas of Lorenz et al., 2014) and elsewhere on Mars. The wavelength of Tharsis' bedforms is more variable, on average form more sinuous patterns (i.e. with higher circular standard deviation, Fig. S12a and c) and most importantly, they present higher HiRISE albedos (Fig. S12b and d). This clearly different albedo signature is further corroborated by plotting the thermal inertias (Putzig and Mellon, 2007) and dust cover index (Ruff & Christensen, 2002) for the mapped areas (Fig. S13). This data shows that the Tharsis bedforms form a distinct population, with lower thermal inertia (possibly denoting finer materials), higher dust coverage/content and morphologies that possess a higher degree of directional variability (the fine "reticulate" texture of the bedforms in this region was previously discussed by Bridges et al., 2010).

The morphology of some of the Tharsis bedforms is also distinctive and variable (e.g. Fig. S14), forming honeycomb patterns or appearing in association with longitudinal spurs/erosive features (Bridges et al., 2010; Lorenz et al., 2014). Tharsis bedforms usually overlay bedrock, forming in some cases extensive mantling units. In contrast, meter-scale bedforms surveyed outside Tharsis typically cover larger scale bedforms (i.e. dark dunes).

The new global survey we present confirms the uniqueness of the bedforms located in the Tharsis region. Tharsis' bedforms were studied in detail by Bridges et al. (2010), proposing that they were formed by saltation of dust aggregates, which in some cases may have produced indurated bedforms. This suggests that major differences in granulometry, density and transport susceptibility exist. Therefore, to test/fit wavelength predictive models Tharsis and non-Tharsis bedforms should be treated separately, as they represent two distinct populations.

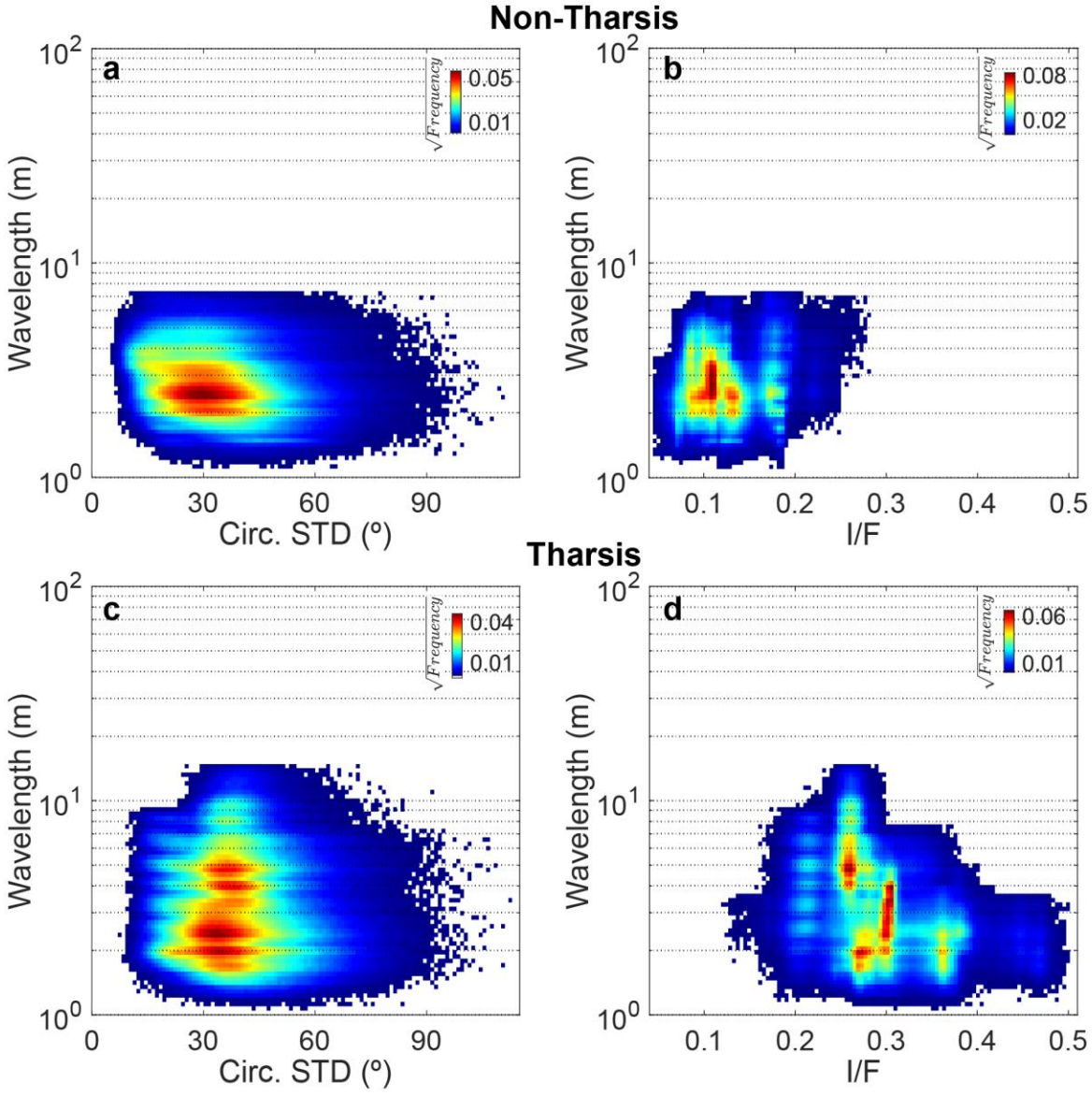

Fig. S12 – 2D histograms of the dark-toned large bedforms mapped in the Tharsis region (c, b) and elsewhere on Mars (a, b). Bedforms in Tharsis show a larger dispersion of wavelengths (clustering at ~2.5 m outside Tharsis and ranging from 1.5-5 m in Tharsis), form patterns with larger trend variations (median circular distributions of ~30º vs. 30-45º) and consistently present higher albedos (<0.25 vs. >0.2).

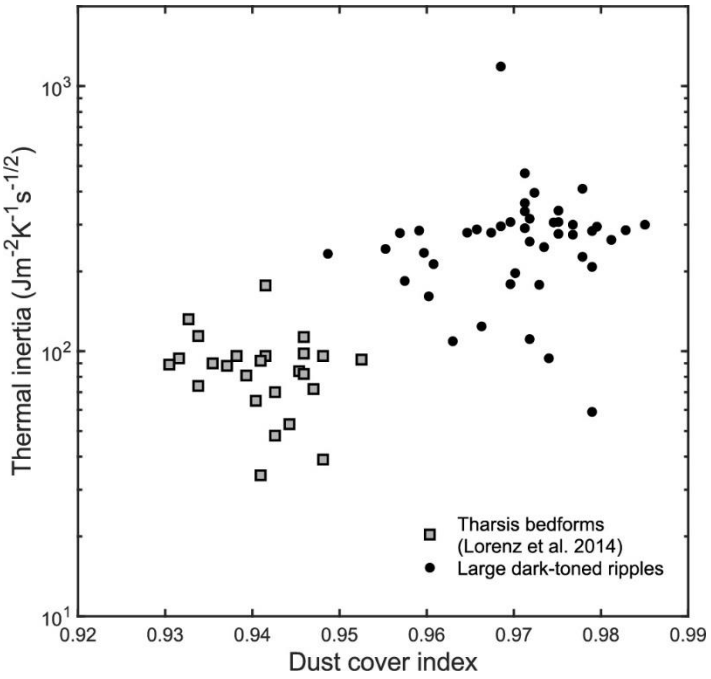

Fig. S13 – Nightside TES thermal inertia (Putzig & Mellon, 2007) **vs. dust cover index** (Ruff & Christensen, 2002) **for all mapped areas. Tharsis areas form a distinct cluster, characterized by lower thermal inertias and lower dust cover index (lower index values are indicative of dust covering, while higher values correspond to dust free areas). This demonstrates that the Tharsis bedforms form a different population, in terms of thermophysical proprieties and dust coverage/content.**

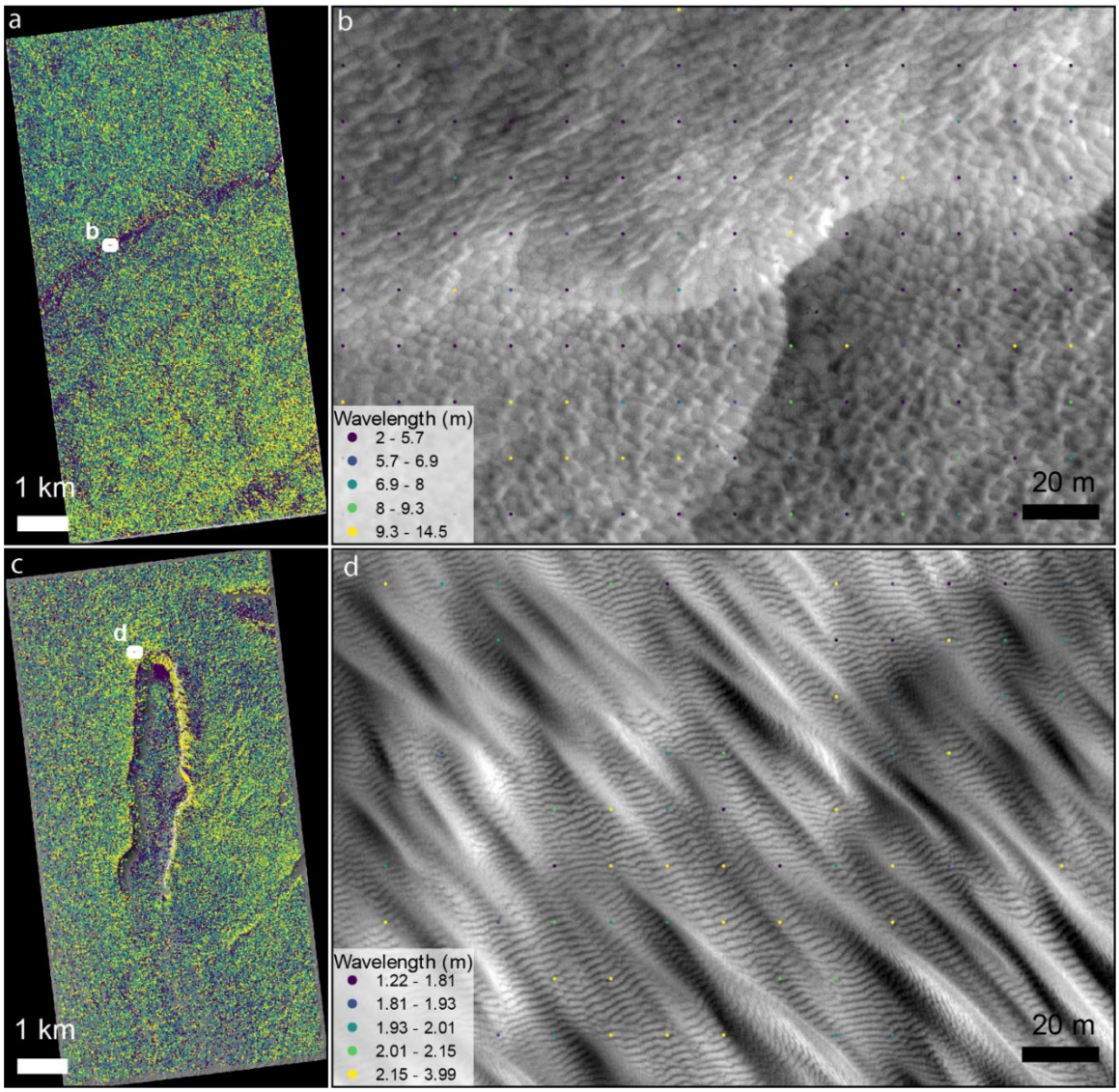

Fig. S14 – Different bedform morphologies in the Tharsis region. a, b) Example of honeycomb shaped bedforms forming a continuous covering unit that encompass all the area (Area 56, PSP_008460_1980). c, d) Transverse linear bedforms that overlay what appear to be erosive longitudinal troughs; also, in this case the bedforms are pervasive, covering almost completely the region and forming a mantling unit that seems to be controlled by the bedrock's main topographic features (Area 72, PSP_010213_1785).

Another point we address here regards the uniformity of the dataset collected outside Tharsis, does our survey include areas which may not be representative of the global trend, i.e. do we have and can we identify possible outliers?

A linear direct relation is evident between average wavelength and elevation (Fig. S15), although a few points do not seem to follow the same trend (the five labelled points

in the plot correspond to the outliers we discuss here). Coincidently, we notice that these five areas have a common attribute: a significant part of the meter-scale bedforms in those areas are located on sand sheets and/or dome dunes.

A closer inspection further revealed other factors that may condition the average measurements for these areas. Namely, in Area 16 (Fig. S16) we have a mixture of two sets of bedforms, one covering barchans and other covering a sand sheet area. The later set presents lower wavelengths which contribute to lower the average wavelength plotted in Fig. S15, producing a noticeable underestimation. Large ripples in Area 34 (Fig. S17) cover low-lying dome dunes or small sand patches located in depressions. This may justify why this area does not follow the same generic trend, as these topographic settings may shelter bedforms and influence their wavelength. Moreover, the assumption of well sorted sediments may not apply in this case, since substantial lag materials may be present in this sediment starved environment. We also note that large ripples in some of the areas identified as outliers are overprinted by dust devil tracks (Fig. S18). This may denote low or even null migration of the bedforms, since the presence of dust devil tracks implies cycles of dust deposition and removal.

To summarize, five areas stand out as outliers, which we associate with cases where sediments may be coarser and poorly sorted, and where active aeolian processes may not be in equilibrium with current day atmospheric conditions. These areas were removed from the subsequent analysis and model fits.

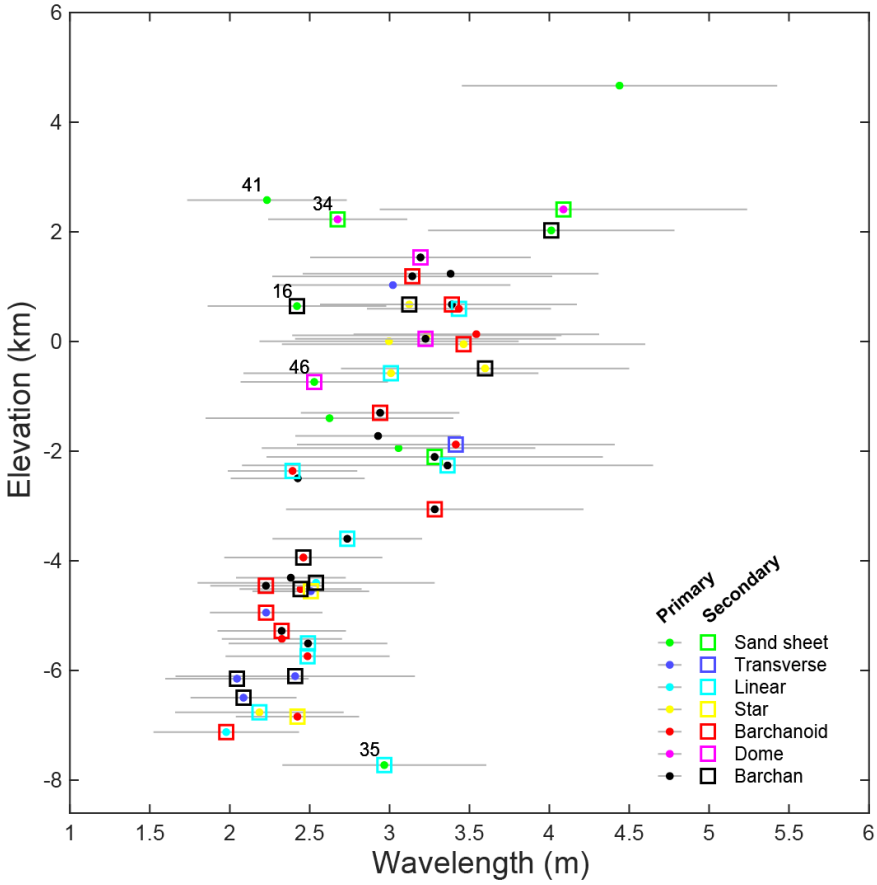

Fig. S15 – Average wavelength vs. elevation for the 50 areas located outside Tharsis, gray lines correspond to 1σ intervals. The color code represents the type of dune morphology present in the mapped areas, when more than one type is present, we assign a primary (covering higher area) and secondary class. The five labeled sites correspond to the outliers discussed in this section.

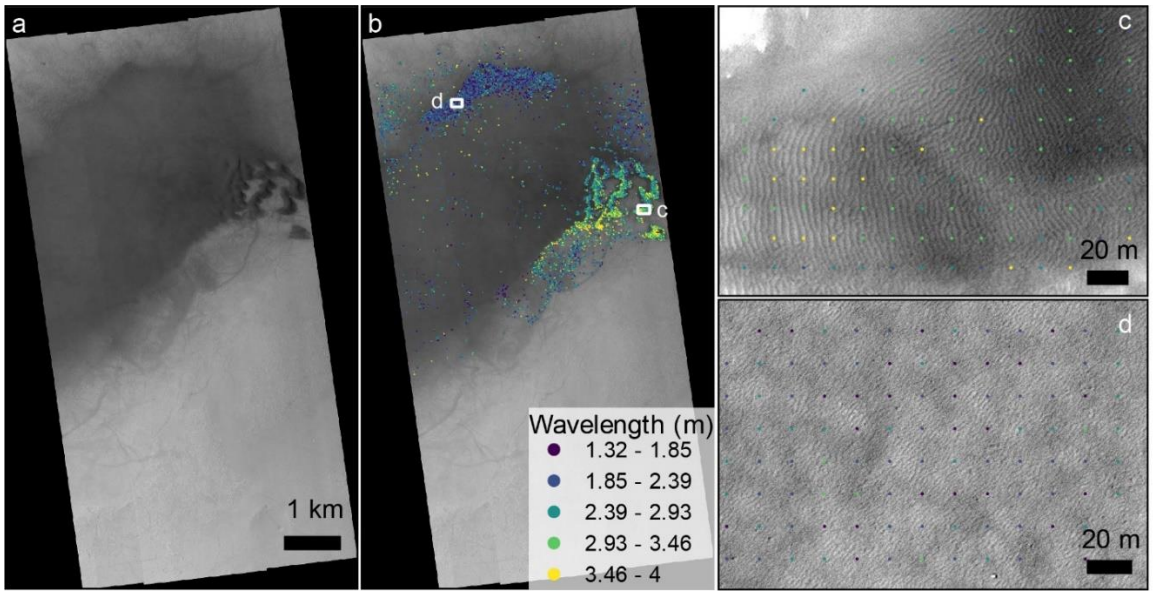

Fig. S16 – Example of a possible outlier where barchans transition to an extensive sand sheet (Area 16). a, b) Wavelength measurements overlaid in the HiRISE image, note the lower wavelengths in the sand sheet (northern section) when compared to the barchans (eastern section). c) Bedforms that cover the barchans, note the presence of dust devil tracks and the higher wavelengths of the ripples. d) Bedforms on the sand sheet present lower wavelengths, therefore the average value for this area merges two different sets of bedforms, with the sand sheet contributing to decreasing the overall wavelength estimate (Fig. S15).

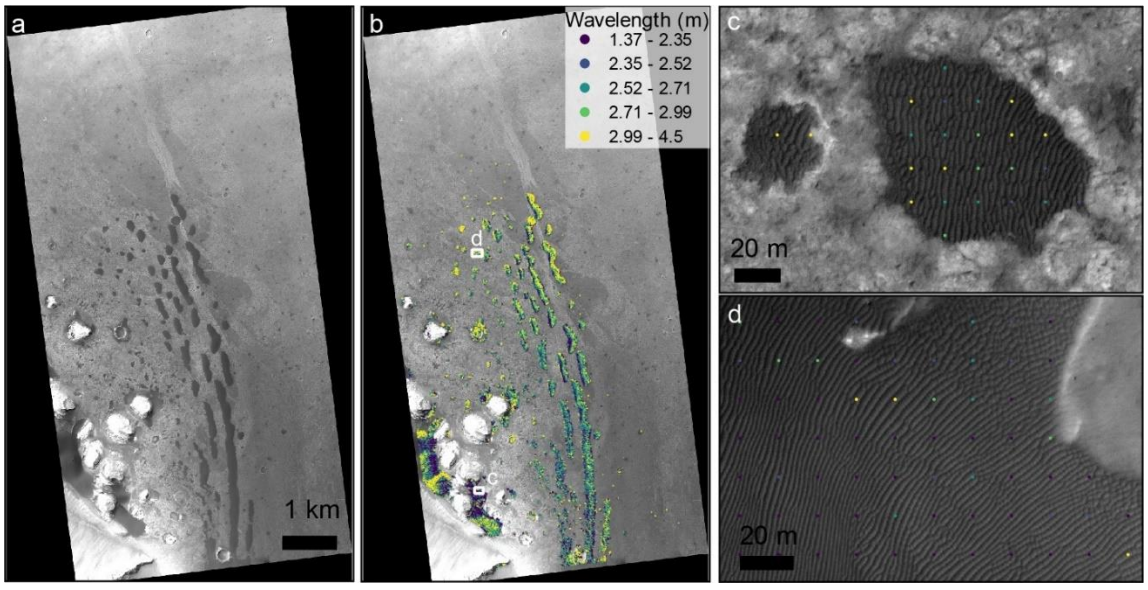

Fig. S17 – Area 34 large ripples cover low-lying dome dunes and sand sheets (ESP_017610_1730), typically located in depressions. We hypothesize that the bedforms in this area may be enriched in coarser/lag materials and that the specific topographic setting may also influence their wavelength. a, b) Wavelength measurements overlaid in the HiRISE image. c, d) large ripples located in crater depressions or other topographic lows.

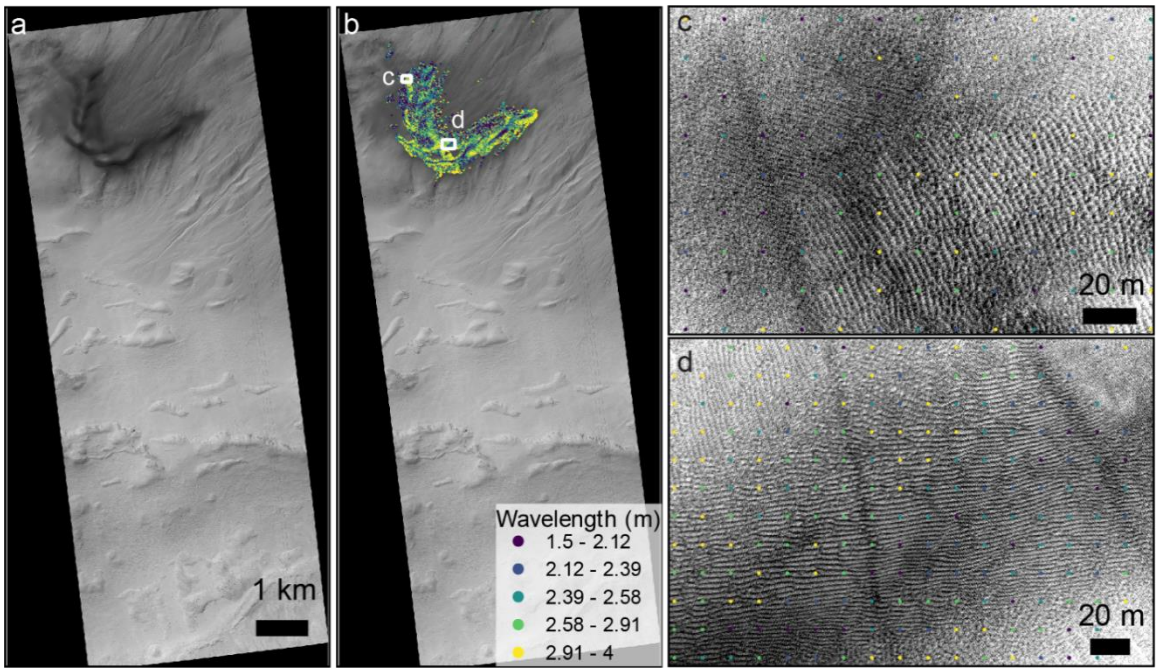

Fig. S18 – Dust devil tracks overlay large ripples in Area 46 (ESP_058788_1320), which implies dust deposition and removal cycles as well as reduced bedform migration. a, b) Wavelength measurements overlaid in the HiRISE image. c, d) Examples of dust devil tracks overlapping the large ripples.

6. WAVELENGTH VS. ATMOSPFERIC DENSITY SCALING: MODELS AND FITS

Here we implemented the same model described in Lapotre et al. (2016), where wind shear velocity (u_*) is set to be equal to the impact threshold shear velocity (u_t) predicted by Kok (2010) model (Table S7 summarizes the models input parameters). Atmospheric density is computed as a function of elevation using the ideal gas law:

$$\boldsymbol{\rho_f(z) = \frac{M_{CO_2}}{r}\frac{p(z)}{T(z)}} \quad \text{(Eq. 3)},$$

where M_{CO2} is the molar mass of carbon dioxide, r is the ideal gas constant and $p(z)$ is the atmospheric pressure computed from MOLA elevations (section 4) using the relation derived from the atmospheric descent profiles of the Mars Exploration Rovers missions (Withers & Smith, 2006). We assume an isothermal atmosphere with a temperature (T) of 227 K, while kinematic viscosity (v) at elevation z is computed through:

$$\boldsymbol{v(z) = \frac{\mu}{\rho_f(z)}} \quad \text{(Eq. 4)},$$

where μ is a constant dynamic viscosity (Table S7).

Based on a fit made to flume experiments and Martian morphometric data, drag ripples' wavelength was predicted to vary according to:

$$\lambda = 2777 \frac{v^{2/3} D^{1/6}}{(Rg)^{1/6} u_*^{1/3}} \qquad \text{(Eq. 5)}$$

where D is grain diameter, g is the gravity acceleration on Mars and R is the submerged reduced density of the sediment ($R = \frac{\rho_s - \rho_f}{\rho_f}$) (Lapotre et al., 2016). This is essentially the same relation later generalized in Lapotre et al. (2017), and is considered to be representative of bedload saturation length (Duran Vinent et al., 2019; Lapotre et al., 2021).

Lapotre et al. (2021) adapted the same framework, considering a saltation saturation length $l_{sat} = \frac{\rho_s u_t^2}{g(\rho_s - \rho_f)}$, which is used to predict bedform wavelength through $\lambda = \frac{\lambda^* v}{u_*}$, where λ^* is a dimensionless wavelength: $\lambda^* \approx 600 \left(\frac{l_{sat} u_*}{v}\right)^{1/3}$ (Lapotre et al., 2021).

In Fig. 3 and S19 we compare our wavelength measurements with the predictions of both models, and we fit power laws and linear models (as proposed by Lorenz et al., 2014) to our datasets.

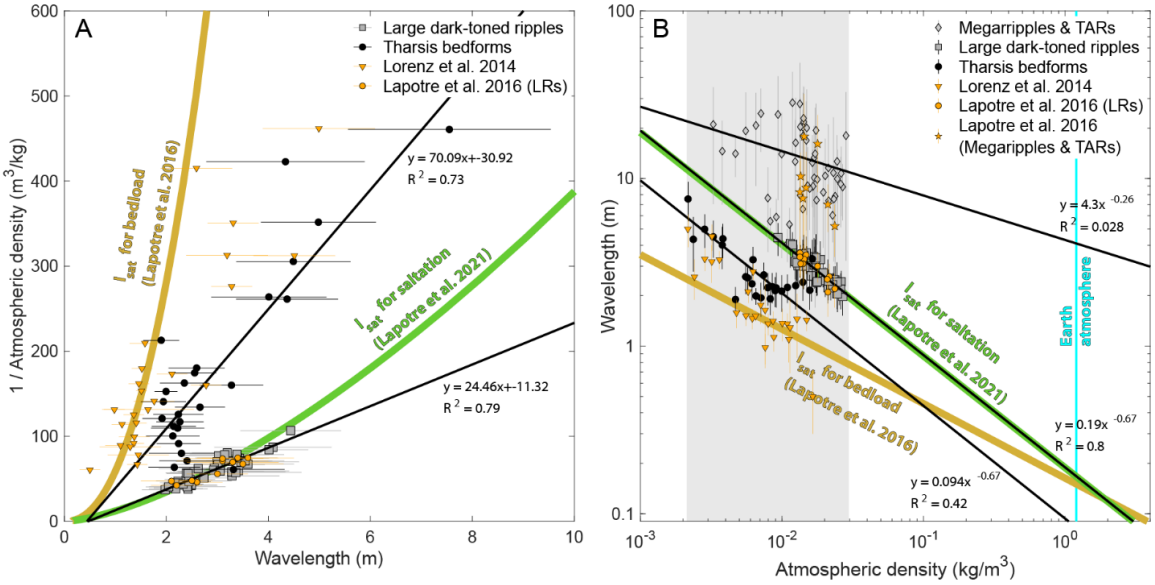

Fig. S20 – Previous surveys and relation between bedforms wavelength and Martian atmospheric density. This is the same plot shown in Fig. 3, where we added the dataset compiled by Lapotre et al. (2016), which includes Lorenz et al. (2014) data for the Tharsis region. We see that a large fraction of this data (corresponding to the Tharsis region bedforms) overlaps the fluid-drag predictions with a bedload saturation length formulation (golden line), while our dataset for these same areas presents higher wavelengths, with the data points located between the two models' predictions. Like in our dataset, the existence of two different clusters is noticeable in the previous compilation, as well as an

overlap of the large ripples datasets with the fluid-drag model predictions when saltation saturation length is considered (green line). The gray area represents the maximum range of atmospheric densities on Mars while the cyan line represents the density of Earth's atmosphere. Black lines represent the best fitted models for the datasets compiled in this study and were computed using the average values for each site (linear models in A and power laws in B; the R^2 values in B were computed in the log space).

Table S7 – Model input parameters.

Variables	Description	Values
M_{CO2}	CO_2 molar mass	44.01 g/mol
r	Ideal gas constant	8.314 $JK^{-1}mol^{-1}$
T	Temperature	227 K
g	Mars gravity acceleration	3.78 m/s^2
σ_s	Grain density (basalt)	2900 kg/m^3
D	Grain diameter	200 µm
µ	Dynamic viscosity	$10.8x10^{-6}$ Pa.s